Icarus 245 (2015) 355–366

Contents lists available at ScienceDirect

Icarus

journal homepage: www.elsevier.com/locate/icarus

Saturn ring rain: Model estimates of water influx into Saturn's atmosphere

L. Moore [a,*], J. O'Donoghue [b], I. Müller-Wodarg [c], M. Galand [c], M. Mendillo [a]

[a] Center for Space Physics, Boston University, Boston, MA 02215, USA
[b] Department of Physics and Astronomy, University of Leicester, Leicester, UK
[c] Space and Atmospheric Physics Group, Imperial College London, London, UK

ARTICLE INFO

Article history:
Received 3 April 2014
Revised 9 July 2014
Accepted 9 July 2014
Available online 30 September 2014

Keywords:
Saturn, atmosphere
Ionospheres
Saturn, rings
Aeronomy

ABSTRACT

Recently H_3^+ was detected at Saturn's low- and mid-latitudes for the first time (O'Donoghue et al. [2013]. Nature 496(7444), 193–195), revealing significant latitudinal structure in H_3^+ emissions, with local extrema in one hemisphere mirrored at magnetically conjugate latitudes in the opposite hemisphere. The observed minima and maxima were shown to map to regions of increased or decreased density in Saturn's rings, implying a direct ring–atmosphere connection. Here, using the Saturn Thermosphere Ionosphere Model (STIM), we investigate the "ring rain" explanation of the O'Donoghue et al. (O'Donoghue et al. [2013]. Nature 496(7444), 193–195) observations, wherein charged water group particles from the rings are guided by magnetic field lines as they "rain" down upon the atmosphere, altering local ionospheric chemistry. Based on model reproductions of observed H_3^+ variations, we derive maximum water influxes of $(1.6–16) \times 10^5$ H_2O molecules cm^{-2} s^{-1} across ring rain latitudes (~23–49° in the south, and ~32–54° in the north), with localized regions of enhanced influx near −48°, −38°, 42°, and 53° latitude. We estimate the globally averaged maximum ring-derived water influx to be $(1.6–12) \times 10^5$ cm^{-2} s^{-1}, which represents a maximum total global influx of water from Saturn's rings to its atmosphere of $(1.0–6.8) \times 10^{26}$ s^{-1}. The wide range of global water influx estimates stems primarily from uncertainties regarding H_3^+ temperatures (and consequently column densities). Future ring rain observations may therefore be able to reduce these uncertainties by determining H_3^+ temperatures self consistently.

1. Introduction

1.1. Water in Saturn's ionosphere

A source of exogenous water has long been inferred at Saturn, particularly as a means to reduce calculated ionospheric densities in order to reproduce observed values. Early Saturn ionospheric models (e.g., McElroy, 1973; Capone et al., 1977) predicted electron densities an order of magnitude larger than those later measured by the Pioneer 11 and Voyager spacecraft (Kliore et al., 1980; Kaiser et al., 1984; Lindal et al., 1985). One chemical effect of introducing oxygen bearing compounds into Saturn's upper atmosphere is to convert H^+ – a long-lived major atomic ion in outer planet ionospheres – into a short-lived molecular ion that quickly dissociatively recombines, thereby reducing the net electron density.

While a number of modeling studies have been able to derive a range of water influxes that adequately explain the Pioneer and Voyager radio occultation measurements (e.g., Connerney and Waite, 1984; Majeed and McConnell, 1991, 1996), directly constraining the influxes observationally has proven more difficult. The first unambiguous direct detection of water in Saturn's upper atmosphere came from the Infrared Space Observatory (ISO; Feuchtgruber et al., 1997), which measured an H_2O column abundance of $(0.8–1.7) \times 10^{15}$ cm^{-2} and was used to derive a global water influx of $\sim 1.5 \times 10^6$ H_2O molecules cm^{-2} s^{-1} (Moses et al., 2000). Subsequent studies based on Submillimeter Wave Astronomy Satellite and Herschel Space Observatory measurements found global influx values within a factor of 2 of the Moses et al. results (Bergin et al., 2000; Hartogh et al., 2011). Despite predictions of latitudinally varying water influxes (e.g., Connerney, 1986), no observational confirmation of such variations has been made to date, with only ambiguous detections of latitudinally varying water concentrations in the ultraviolet (e.g., a 2σ-detection of 2.70×10^{16} cm^{-2} at 33°S latitude: Prangé et al., 2006), and preliminary indications of larger equatorial water densities from Cassini Composite InfraRed Spectrometer (CIRS) observations (Bjoraker et al., 2010).

* Corresponding author.

http://dx.doi.org/10.1016/j.icarus.2014.08.041
0019-1035/

A counter-intuitive trend in electron density with latitude was revealed after the arrival of Cassini at Saturn, based on the 31 new radio occultation measurements published to date (Nagy et al., 2006; Kliore et al., 2009). Despite being near Saturn's equinox, with the sun directly overhead at low-latitudes, electron densities were found to be lowest at Saturn's equator and to increase with latitude, a behavior that Moore et al. (2010) were able to reproduce by introducing a water influx that peaked at Saturn's equator and decreased with latitude. Such a water influx profile is in agreement with predictions by models investigating the evolution of Enceladus' water vapor plumes (Jurac and Richardson, 2007; Cassidy and Johnson, 2010; Fleshman et al., 2012). While a ring-derived ionized influx may yet be present, there are only five published Cassini radio occultations at latitudes that map magnetically to Saturn's rings, and therefore there is insufficient latitudinal resolution in the electron density observations to clearly identify any of the expected local extrema that would result from possible ring-derived influxes.

1.2. Saturn ring rain observations

Recently H_3^+ was detected at Saturn's low- and mid-latitudes for the first time (O'Donoghue et al., 2013), revealing significant latitudinal structure in H_3^+ emissions, with local extrema in one hemisphere mirrored at magnetically conjugate latitudes in the opposite hemisphere. Furthermore, the observed minima and maxima were shown to map to regions of increased or decreased density in Saturn's rings, implying a direct ring–atmosphere connection. The H_3^+ ion has a relatively short chemical lifetime; its dominant loss process is dissociative recombination with electrons. While oxygen bearing compounds such as OH and H_2O have typically been introduced into models of Saturn's ionosphere as a means of reducing the electron density through charge exchange with H^+, they also impact H_3^+ densities, primarily by reducing dissociative recombination rates. Therefore, the sharp latitudinal structures observed by O'Donoghue et al. (2013) – which cannot be explained by solar ionization effects – likely represent a proxy for external oxygen influxes (Connerney, 2013). Here, using the Saturn Thermosphere Ionosphere Model (STIM), we estimate the upper limits for ring-derived atmospheric ion influxes implied by the ring rain observations, and we use those values to derive lower limits on ring mass loss rates.

2. Methods

2.1. Ring ion influx

Saturn's rings are composed primarily of water ice bodies (e.g., Cuzzi et al., 2010 and references therein) between 1 cm and 20 m in size (Zebker et al., 1985; French and Nicholson, 2000). Solar UV photon-induced decomposition of ice leads to the production of an O_2 ring atmosphere, which can accumulate both above and below the ring plane due to a long lifetime and frequent interactions with ring particles (Johnson et al., 2006). Two Cassini instruments detected a ring ionosphere during Cassini's orbital insertion in 2004, finding evidence of O^+ and O_2^+ ions (Tokar et al., 2005; Waite et al., 2005), likely the result of photoionization of O_2. Models of Saturn's ring ionosphere support the dominance of O^+ and O_2^+, and further find that within the radius where Keplerian and corotation velocities are equal in the ring plane, $\sim 1.8 R_S$, ring ions spiral along magnetic field lines and precipitate into Saturn's atmosphere with near unit efficiency. Outside of this radius initially trapped ions can also later be scattered into the loss cone (Luhmann et al., 2006; Tseng et al., 2010). Therefore, as O_2^+ and O^+ are the dominant ring ionosphere ions, they are also the ring-derived ions most likely to precipitate into Saturn's atmosphere.

As O_2^+ ions dissociatively recombine with electrons extremely rapidly – roughly three times faster than H_3^+ ions in Saturn's ionosphere – any precipitating O_2^+ will lead to a chain of photochemical reactions that produce primarily OH (via $O + H_2$) and H_2O (via $OH + H_2$) in the thermosphere and lower atmosphere (e.g. Moses et al., 2000). An influx of H_2O or H_2O^+ would lead to similar chemistry, as the products of dissociative recombination reactions between H_3O^+ (formed rapidly from H_2O^+) and electrons include OH and H_2O. In other words, an external flux of neutrals (e.g., H_2O) or ions (e.g., O_2^+) can lead to similar number densities of oxygen-bearing molecules in Saturn's atmosphere, and it is these molecules that charge-exchange with H^+. The subsequent rapid dissociative recombination of the resulting charge-exchange products (e.g., H_3O^+) then leads to the required reduction in Saturn's electron densities and the subsequent decrease in H_3^+ chemical loss rates. The most important remaining distinction between ionized and neutral influxes is their deposition latitude, as ions are constrained to precipitate along magnetic field lines. Therefore, in order to maintain consistency with previous Saturn ionospheric literature, we treat the ring rain influx inferred from H_3^+ observations here as a "water" influx. In this way derived fluxes can be compared directly with previous results, and the language of this text is simplified. Finally, it should be noted that water from Saturn's rings may also be more efficiently transported in the form of charged sub-micrometer grains rather than ions (e.g., Connerney, 2013), a possibility that remains to be evaluated.

2.2. Temperatures in Saturn's upper atmosphere

The observations of O'Donoghue et al. (2013) report the intensity of H_3^+ emission (in nW m^{-2}) versus planetocentric latitude. (All latitudes quoted in this manuscript are planetocentric unless specified otherwise.) In order to compare those observations with model results, a conversion between intensity and vertical column content is required. Typically, the intensity of two or more discrete ro-vibrational spectral lines of H_3^+ can be used to determine its temperature and subsequently its density (Miller et al., 2000). The O'Donoghue et al. observations unfortunately lacked sufficient signal-to-noise to carry out such a derivation. Therefore, in order to estimate the H_3^+ temperatures that correspond with the ring rain observations, we follow a three step process: (1) determine the most realistic representation of the behavior of neutral exospheric temperature with planetocentric latitude, $T_{exo}(\phi_{pc})$, based on ultraviolet solar and stellar occultations; (2) use STIM to find the temperature differential between the exobase and the altitude of H_3^+ ions (typically $\sim$2700–3000 km and $\sim$1200 km above the 1 bar pressure level at Saturn, respectively); and (3) apply the STIM temperature differential to a functional form of $T_{exo}(\phi_{pc})$ (see below), yielding neutral temperature predictions at H_3^+ altitudes, $T_{H_3^+}(\phi_{pc})$.

Early Voyager analyses of solar and stellar occultations suggested that Saturn's exospheric temperature could be as high as 850 K (Broadfoot et al., 1981; Festou and Atreya, 1982). However, subsequent Voyager 2 reanalyses found a temperature closer to 420 K (Sandel et al., 1982; Smith et al., 1983), a value also supported by modern reanalyses of occultations by both Voyager spacecraft (Vervack and Moses, submitted for publication). Given the limited number of Voyager observations and the uncertainties in analyzing them, it was not possible to use them to construct a complete latitudinal trend for Saturn upper atmospheric temperatures. However, recent analyses of 15 solar (Koskinen et al., 2013) and 3 stellar (Shemansky and Liu, 2012) occultations by Cassini, in combination with previous Voyager results, now allow for a more realistic estimate of the behavior of upper atmosphere temperature with latitude.

Fig. 1 presents the upper atmosphere temperature measurements described above (aside from the values above 800 K), as well

as some auroral H_3^+ temperature measurements (Melin et al., 2007, 2011; O'Donoghue et al., 2014), a neutral temperature proxy at lower altitudes. Different symbols represent the references highlighted in the figure legend, gray vertical lines indicate quoted or estimated temperature uncertainties, and the gray shaded regions highlight the latitudes of ring rain observations (from Fig. 2 of O'Donoghue et al., 2013). Fig. 1 also presents a number of different methods for deriving $T_{exo}(\phi_{pc})$ from the measurements. Orange and green lines result from least square fits to the function $T_{exo}(\phi_{pc}) = A_1 \sin^2\phi_{pc} + A_2 \cos^2\phi_{pc}$, where A_1 and A_2 are constants that vary according to the combinations of datasets that have been included in each fit (as indicated by the numbers in brackets). These curves are labeled as S0 and S1, and will be referred to using those designations for the remainder of the text. The dotted line is for a linear least squares fit (fit L1), while the dashed line represents the global arithmetic mean T_{exo} (i.e., assumed constant with latitude; fit M1). Data points are weighted by the inverse square of their uncertainties in order to derive the various fits. Finally, cyan and purple lines correspond to the maximum and minimum temperatures from the above fits, respectively, within the ring rain latitude regions (fits T_{MAX} and T_{MIN}).

Two main points should be emphasized from Fig. 1. First, there is the drastic difference in $T_{exo}(\phi_{pc})$ profiles between fits that do and do not include the Cassini solar occultations values (Koskinen et al., 2013). These are labeled as reference [6] in the figure legend, and their dominance in derivations of meridional temperature trends emphasizes their value in understanding the energetics of Saturn's upper atmosphere. Second, despite the additional insight brought by the Cassini occultations, there remains significant uncertainty and/or variability in global thermospheric temperature determinations. It is, perhaps, not surprising that there is no obvious global trend in neutral temperature, as measurements span a range of seasonal and solar conditions at Saturn. Different researchers may well favor different methods for constructing a "true" global thermospheric temperature behavior from the limited available data. Therefore, the cyan and purple lines, representing a maximum and minimum temperature at ring rain latitudes, respectively, will be used to illustrate how different choices regarding ring rain exospheric temperatures would affect the subsequent results, such as estimated H_3^+ column densities and ring-derived water influxes.

Some additional discussion regarding the choice of fits in Fig. 1 is worthwhile. First, H_3^+ temperatures would ideally be taken directly from H_3^+ observations. Unfortunately, previous measurements of H_3^+ temperatures are only available at auroral latitudes, and therefore do not provide adequate insight into temperatures at ring rain latitudes. Moreover, as H_3^+ temperature measurements sample a lower altitude region than the UV temperature measurements, additional assumptions regarding IR-UV temperature differentials would be necessary to include them in any global temperature fit. Instead, the available H_3^+ temperature measurements are included in Fig. 1 for completeness, and for comparison with UV temperature measurements. Second, the Cassini stellar occultation results of Shemansky and Liu (2012) have been omitted from the temperature fits of Fig. 1 due to the lack of published uncertainty for the βCru occultation at −3.6° latitude (blue triangles in Fig. 1). If an uncertainty of 10 K were assumed for the βCru measurement – midway between the 5 K and 15 K uncertainties reported at −42.7° and 15.2° latitude (Shemansky and Liu, 2012) – then a sinusoidal fit using references [1], [4], [5] and [6] would yield a temperature profile roughly constant with latitude, near 460 K, and well within the temperature range between the cyan and purple lines of Fig. 1.

Observed ro-vibrational infrared emissions from the H_3^+ ion are dependent on temperature and density of the emitting gas. Neutral temperature in Saturn's thermosphere starts at a lower boundary value of ~150 K near the homopause (e.g., Hubbard et al., 1997), and increases toward an isothermal value (the "exospheric temperature") in the upper thermosphere. As H_3^+ is expected to be in quasi-thermal equilibrium with the surrounding gas in the outer planets at lower altitudes (Miller et al., 1990; Moore et al., 2008), its emissions are thus a good proxy for neutral temperatures over the altitude regions where H_3^+ densities peak. Ionospheric models predict the altitude of maximum H_3^+ density to be between ~1000 and 1400 km, depending on solar and seasonal conditions and latitude (Majeed and McConnell, 1996; Moses and Bass, 2000; Moore et al., 2009). Recently, the auroral H_3^+ emission was observed to peak near 1155 km (Stallard et al., 2012), essentially coincident with a previously measured UV auroral emission altitude (Gérard et al., 2009). Therefore, at least in auroral regions, measured H_3^+ temperatures appear to primarily sample temperatures in the lower thermosphere, and are expected to be up to 50 K cooler than the corresponding exospheric temperatures (Müller-Wodarg et al., 2012).

In order to convert the $T_{exo}(\phi_{pc})$ profiles derived in Fig. 1 into H_3^+ temperature profiles we turn to the $T_{exo}(\phi_{pc}) - T_{H_3^+}(\phi_{pc})$ temperature differentials calculated by the Saturn Thermosphere Ionosphere Model (STIM; Müller-Wodarg et al., 2012). STIM is a

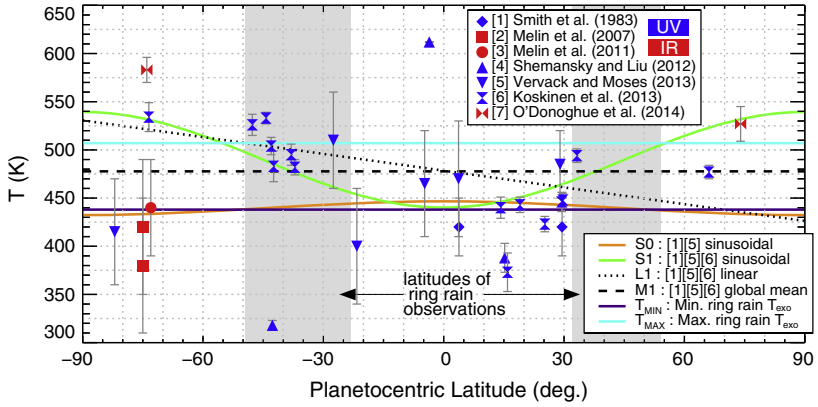

Fig. 1. Symbols represent thermospheric temperature measurements from ultraviolet stellar and solar occultations – references [1], [4], [5], [6], blue symbols – and from auroral infrared H_3^+ observations – references [2], [3], and [7], red symbols. Curves indicate global temperature fits that weight the data points by the inverse square of their uncertainties. Green and orange lines (fits S0 and S1) assume a functional form $A_1 \sin^2\phi_{pc} + A_2 \cos^2\phi_{pc}$, the dotted curve is for a linear fit (L1), and the dashed curve is the global mean temperature (M1). Cyan and purple lines correspond to the maximum and minimum temperatures from the fits at ring rain latitudes, indicated by gray shaded regions. (For interpretation of the references to color in this figure legend, the reader is referred to the web version of this article.)

General Circulation Model (GCM) that treats the global response of Saturn's upper atmosphere to solar and auroral forcing. Key physical quantities calculated in STIM include neutral temperatures, neutral and ion densities, neutral winds, and ion drifts. Fig. 2 shows STIM calculations of the difference in neutral temperature between the H_3^+ peak altitude and the exobase as a function of latitude. These values are based on the conditions of STIM simulation R15 (see Table 1 of Müller-Wodarg et al., 2012), a representative case for average levels of magnetospheric forcing that reproduces observed auroral temperatures. R15 solar and seasonal conditions are minimum and equinox, respectively. It includes imposed electric fields with peak strength of 76 mV m^{-1}, and allows for a local time averaged auroral particle precipitation flux of 0.62 mW m^{-2} of 10 keV electrons. By applying the temperature differential profile of Fig. 2 to the exospheric temperature profiles of Fig. 1, we can thus derive estimates of H_3^+ temperature as a function of latitude.

2.3. Estimation of H_3^+ column densities from ring rain observations

Under conditions of local thermodynamical equilibrium, the energy emitted by a molecule of H_3^+ during a single ro-vibrational transition is given by Stallard et al. (2002):

$$I_{calc}^{mol.} = \frac{g(2J+1)hc\omega A \exp\left[\frac{-E'}{kT}\right]}{4\pi Q(T)} \quad (1)$$

where $I_{calc}^{mol.}$ (in W str^{-1} molecule^{-1}) is the intensity of a given H_3^+ ro-vibrational transition line at temperature T and at wavenumber ω. The nuclear spin degeneracy is given as g, J is the angular momentum of the molecule, A is the Einstein A-coefficient for spontaneous emission, E' is the upper energy level of the transition, h and k are the Planck and Boltzmann constants, respectively, and c is the speed of light. $Q(T)$ is the partition function at temperature T, for which updated coefficients are given by Miller et al. (2010). These line parameters have been calculated ab initio by Neale et al. (1996). Multiplying Eq. (1) by the column density of emitting H_3^+, $N_{H_3^+}$, yields the total observed flux at wavenumber ω for constant temperature T:

$$I_{obs} = I_{calc}^{mol.}(T) N_{H_3^+} \quad (2)$$

This is the value reported by O'Donoghue et al. (2013) in their ring rain observations. First principles calculations, represented here by $I_{calc}^{mol.}$, are the means by which H_3^+ column densities can be derived from observed ro-vibrational spectral line intensities. Typically this calculation is performed after the temperatures are first determined from observed spectral line intensity ratios (e.g., Melin et al., 2011). However, as the O'Donoghue et al. detections are too weak to derive temperatures directly, in this work we must use the temperatures estimated in Section 2.2.

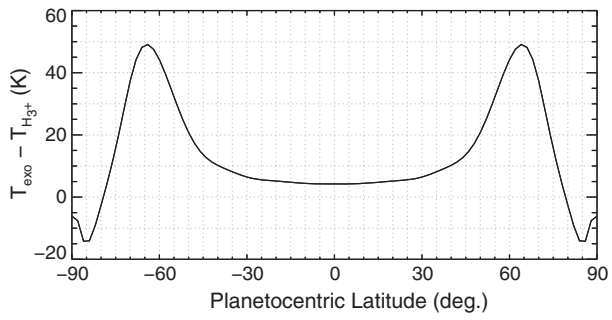

Fig. 2. Difference in neutral temperature between the H_3^+ peak altitude and the exobase, as calculated by STIM (Müller-Wodarg et al., 2012).

In order to streamline the process of calculating $N_{H_3^+}$ for 40 different ring rain latitude elements (O'Donoghue et al., 2013) across a wide range of different temperatures, we first develop a parameterization that links H_3^+ column density, temperature and observed intensity. This parameterization comes from previous first principles calculations of H_3^+ emission based on a wide range of STIM-generated atmospheres spanning neutral temperatures from ~400 to 800 K (Fig. 12 and associated text of Müller-Wodarg et al., 2012), and is tailored for the $Q(1,0^-)$ line at 3.953 μm. It is given as:

$$N_{H_3^+} = \frac{1}{T_{H_3^+}^4} \exp\left\{\frac{(\ln I_{H_3^+} + 87.40)}{1.167}\right\} \quad (3)$$

where $N_{H_3^+}$ is column density in m^{-2}, $T_{H_3^+}$ is temperature in K, and $I_{H_3^+}$ is the $Q(1,0^-)$ line intensity in W m^{-2} str^{-1}.

In combination with the temperature profiles of Figs. 1 and 2, and the $Q(1,0^-)$ line intensities shown in Fig. 2 of O'Donoghue et al. (2013), Eq. (3) allows a direct calculation of the observed H_3^+ column density as a function of latitude, shown in Fig. 3. In order to estimate the maximum H_3^+ column densities, the maximum observed $Q(1,0^-)$ line intensities are used (i.e., full 3-sigma offset from the profile shown in Fig. 2 of O'Donoghue et al., 2013). As in Fig. 1, the orange and green curves (S0 and S1) assume a smoothly varying global temperature behavior, while the dotted curve (L1) assumes a linear behavior with latitude, and the dashed curve (M1) uses the global mean temperature, constant with latitude. The jaggedness of the profiles shown in Fig. 3 represents the latitude resolution in the O'Donoghue et al. (2013) observations. By comparing modeled H_3^+ column densities with those of Fig. 3, we will be able to place constraints on possible ring-derived water influxes that could give rise to the observed structure. Higher estimated H_3^+ temperatures correspond to smaller calculated column densities. The purple and cyan curves in Fig. 3 (T_{MIN} and T_{MAX}), therefore, outline a range of minimum and maximum H_3^+ column densities in that any assumed thermospheric temperature profiles that fall within the temperature range indicated in Fig. 1 would yield H_3^+ column density estimates between the cyan and purple curves of Fig. 3.

2.4. Ionospheric chemistry

In order to match observed electron densities, models must convert H^+ – a dominant and long lived atomic ion in Saturn's ionosphere – into a short lived molecular ion. The two most commonly considered chemical loss pathways for H^+ are:

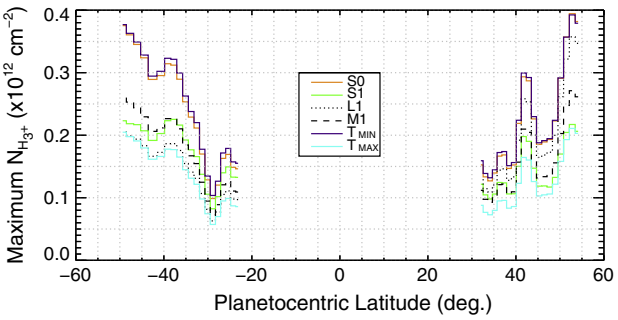

Fig. 3. Maximum Saturn ring rain H_3^+ column densities estimated from Eq. (3), using observed $Q(1,0^-)$ spectral intensities and uncertainties at 3.953 μm (Fig. 2 of O'Donoghue et al., 2013), H_3^+ temperature profiles based on observed exospheric temperatures (Fig. 1), and modeled temperature differentials (Fig. 2). The identifiers in the legend refer to temperature fits from Fig. 1.

Water pathway

$$H^+ + H_2O \rightarrow H_2O^+ + H \quad (4)$$

$$H_2O^+ + H_2 \rightarrow H_3O^+ + H \quad (5)$$

$$H_3O^+ + e \rightarrow \begin{matrix} H_2O + H \\ OH + 2H \end{matrix} \quad (6)$$

Vibrationally excited H_2 pathway

$$H^+ + H_2(v \geqslant 4) \rightarrow H_2^+ + H \quad (7)$$

$$H_2^+ + H_2 \rightarrow H_3^+ + H \quad (8)$$

$$H_3^+ + e \rightarrow \begin{matrix} 3H \\ H_2 + H \end{matrix} \quad (9)$$

While the water-group process of ion and electron removal via reactions (4)–(6) has been discussed already in Section 2.1, it is worth noting that other oxygen bearing compounds (such as OH) could perform a similar function, with the effective loss rate being driven by the analog to reaction (4).

An alternative method of reducing H^+ densities, reaction (7), is exothermic only when H_2 is excited to the 4th or higher vibrational state (McElroy, 1973). The reaction rate for (7) is thought to be near its maximum kinetic rate (e.g., Huestis, 2008; Huestis et al., 2008); however the population of vibrationally excited molecular hydrogen, $H_2(v \geqslant 4)$ – hereafter H_2^* – is to date not constrained by observations. Assumed abundances of H_2^* vary by over 4 orders of magnitude in model reproductions of radio occultation observations (Majeed et al., 1990, 1991; Majeed and McConnell, 1991; Moses and Bass, 2000). Furthermore, there are only two (related) first principles calculations of H_2^* at Saturn (Majeed et al., 1990, 1991). All later ionospheric studies have used various parameterizations that either derived an H_2^* distribution based on a single assumed vibrational temperature (Majeed and McConnell, 1991, 1996; see also Cravens, 1987), or have modified the calculated distributions of H_2^* by Majeed et al. (1991) in some fashion (e.g., Moses and Bass, 2000; Moore et al., 2006, 2010). In short, at present H_2^* is an unconstrained parameter at Saturn, and must be treated as such along with the external water influx.

2.5. Modeling approach

For this work we use a 1-D ionospheric module of STIM that solves the ion continuity and momentum equations over a fixed neutral background (Moore et al., 2004, 2008), taken from the 3-D STIM GCM (Müller-Wodarg et al., 2012). This approach is necessary in order to fully explore the possible parameter space of water influxes and H_2^* populations with sufficient precision; it would be computationally prohibitive to treat the $>10^5$ model runs performed here in full 3-D. However, this approach is also justified by the goal of performing H_3^+ model-data column density comparisons, as the short chemical lifetimes for H_3^+ ions at Saturn mean they are firmly in the photochemical regime, and therefore relatively insensitive to global dynamics. In order to generate neutral atmospheric profiles that correlate with the temperatures described in Section 2.1, temperatures are fixed at ~135 K at the base of the thermosphere, and then scaled to the exospheric temperatures derived in Fig. 1 while retaining the qualitative vertical thermal structure calculated within STIM. In similar fashion, neutral densities are fixed at the homopause and then scaled vertically using scale heights appropriate for the observed temperatures (and using the latitudinal temperature profiles of Fig. 1). Water density altitude profiles are based on time-dependent diffusion calculations that include constant topside water influx as a boundary condition (Moore et al., 2006; Moore and Mendillo, 2007).

Model calculations rely on solar EUV and X-ray fluxes specified using measurements from the Thermosphere Ionosphere Mesosphere Energetics and Dynamics Solar EUV experiment (TIMED/SEE: Woods et al., 2000, 2005; Woods, 2008). Solar fluxes have been extrapolated to Saturn for 17 April 2011, the date of the ring rain observations (O'Donoghue et al., 2013), with a corresponding F10.7 radio flux index of 114.4, and a sub-solar latitude at Saturn of 9.1°.

In order to account for the uncertain water influxes and H_2^* distributions, we explore a wide range of each in order to find the combination of parameters that best reproduces the H_3^+ column densities derived from ring rain observations (Fig. 3). A sample of such a series of model results is shown in Fig. 4, which gives the calculated H_3^+ column density at noon – the local time of ring rain observations – as a function of water influx, Φ_{H_2O}, and H_2^* population, represented here as k_{fac}. (As the model solves ion continuity and momentum equations via explicit time integration, results are available for all local times, though only noon values are shown unless otherwise specified.) The effective reaction rate for (7), k_{eff}, is taken to be a multiplicative factor (k_{fac}) of the Moses and Bass (2000) rate, k_{MB2000} (see also Majeed et al., 1991), and represents a combination of the chemical reaction rate, k_7, and the fraction of vibrationally excited H_2, $H_2(v \geqslant 4)/H_2$. Similar model simulations are undertaken for all 40 of the ring rain latitude elements,

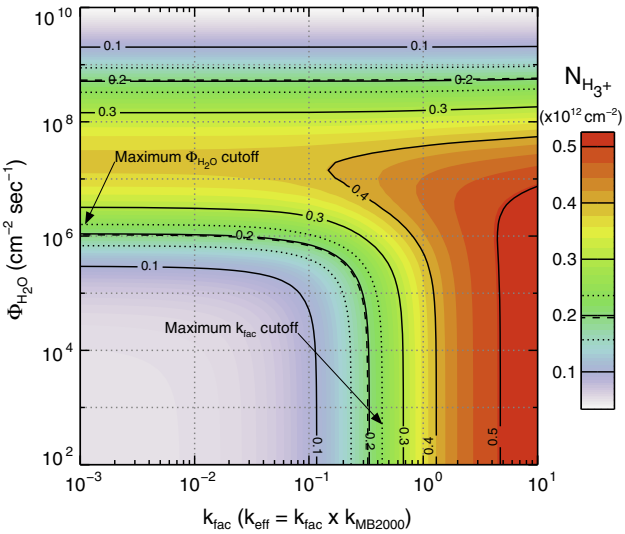

Fig. 4. Contours of modeled H_3^+ column densities for a range of water influxes, Φ_{H_2O}, and populations of vibrationally excited H_2, represented here by k_{fac} (see text). Calculation results are for −35° latitude and a solar local time of noon. The dashed curves indicate the H_3^+ column density derived from ring rain observations at −35° latitude, based on the green profile (S1) from Fig. 3, and therefore identify the combinations of Φ_{H_2O} and k_{fac} parameters that can reproduce the observation at that latitude. Dotted curves outline the range of estimated H_3^+ column densities that result from accounting for a 3-sigma uncertainty in observed H_3^+ emission intensity (i.e., Fig. 2 of O'Donoghue et al., 2013). Maximum Φ_{H_2O} and k_{fac} cutoffs are indicated by arrows (see text). (For interpretation of the references to color in this figure legend, the reader is referred to the web version of this article.)

thereby exploring an identical parameter space for different solar zenith angles and neutral background atmospheres.

There are two important patterns to note in Fig. 4. First, for water influxes above $\sim 10^5$ cm^{-2} s^{-1}, calculated H_3^+ column densities initially increase and then eventually decrease as more and more water is introduced into Saturn's ionosphere (above $\sim 2 \times 10^7$ cm^{-2} s^{-1}). In other words, water can act as both a "source" and a sink for H_3^+. This apparent anomaly is easily explained by the fact that the dissociative recombination rate of H_3^+ is relatively fast and therefore a reduction in modeled electron densities, such as the one resulting from the $H^+ + H_2O$ charge exchange reaction chain (4)–(6), leads to a corresponding reduction in the $H_3^+ + e^-$ loss process. In addition, for most values of k_{fac}, there is a maximum modeled H_3^+ column density for a water influx of $\sim 2 \times 10^7$ cm^{-2} s^{-1}. Second, an increase in k_{fac} represents an increase in the effective rate for the $H^+ + H_2(v \geqslant 4)$ reaction, and hence an increase in the production of H_3^+ via reaction (8). Consequently modeled H_3^+ column densities are always larger than observed densities for k_{fac} values of ~ 1 or more and water influxes of $\sim 10^7$ cm^{-2} s^{-1} or less. At extremely large values of external water influx, above 10^8 cm^{-2} s^{-1}, there is insufficient H^+ for reaction (7) to play any further significant role, and water chemistry dominates calculated H_3^+ densities.

Fig. 5 presents model results for the same range of parameters explored in Fig. 4, except it shows electron column densities at dawn rather than H_3^+ column densities at noon. In this way the measured electron column density from Cassini radio occultation 047x (Table 1 of Kliore et al., 2009) – indicated by the dashed curve – can be compared with the model results. Occultation 047x is chosen as a typical representative of the 5 total Cassini radio occultations at ring rain latitudes (047x, 051n, 051x, 070n, and 072n), as it is at approximately −35° planetocentric latitude, and therefore can easily be compared with the conditions of Fig. 4. It should be noted that, while radio occultations sample a range of latitudes – e.g., 36.7S to 41.2S planetographic latitude for 047x – the majority of the electron column content associated with a particular occultation is generated in the lower ionosphere, near the electron density peak, and therefore near the end of the quoted latitude range (e.g., 41.2S for 047x). Finally, it is most likely a coincidence that similar combinations of Φ_{H_2O} and k_{fac} appear capable of reproducing the observed H_3^+ and electron column densities in Figs. 4 and 5, respectively, as the observations were made under very different seasonal and solar conditions.

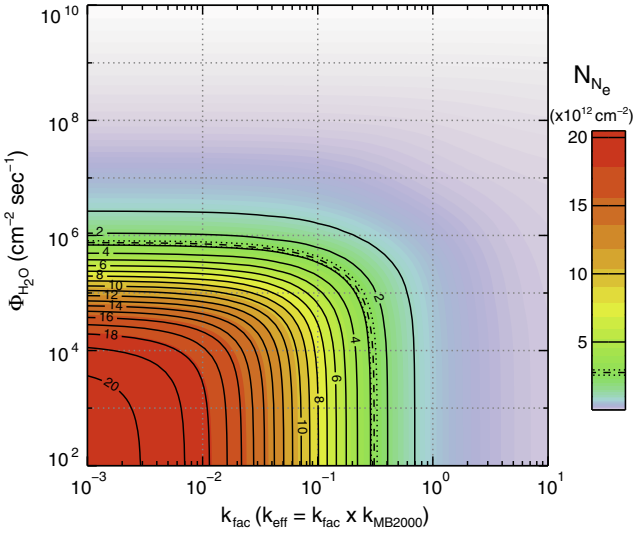

Fig. 5. Contours of modeled electron column densities for a range of water influxes, Φ_{H_2O}, and populations of vibrationally excited H_2, represented here by k_{fac} (see text). Calculation results are for −35° latitude and a solar local time of dawn. The dashed curve indicates the electron column density derived from Cassini radio occultation observation 047x at −41.2° planetographic latitude (Kliore et al., 2009; Moore et al., 2010), or approximately −35° planetocentric latitude. Dotted curves represent a possible 3-sigma range of observed electron column densities, determined by applying the maximum uncertainty quoted Nagy et al. (2006), as no uncertainties are reported in Kliore et al. (2009).

Both Figs. 4 and 5 reveal an interesting behavior: for small values of Φ_{H_2O}, modeled column densities increase (H_3^+) or decrease (N_e) monotonically with increasing k_{fac}. A similar behavior is found for small values of k_{fac}, with the exception that modeled H_3^+ column densities maximize near 2×10^7 cm^{-2} s^{-1}, and then decrease again for larger water influxes. In other words, based solely on Fig. 4, there are two families of Φ_{H_2O} and k_{fac} values that are capable of reproducing observed H_3^+ column densities, a "low" water influx solution ($\Phi_{H_2O} < 10^7$ cm^{-2} s^{-1}) and "high" water influx solution ($\Phi_{H_2O} > 10^8$ cm^{-2} s^{-1}). By making use of the model results of Fig. 5, however, we can exclude the high water influx solution, as the modeled electron densities there are far too small when compared with radio occultation measurements. The electron column densities from the 5 Cassini radio occultations that overlap with ring rain latitudes – 047x, 051n, 051x, 070n, and 072n – are 2.76, 1.76, 2.41, 1.66, and 1.64, respectively (in units of 10^{12} cm^{-2}; Kliore et al., 2009; Moore et al., 2010). All of these values lie within the outermost solid contour of Fig. 5.

Therefore, by focusing on model comparisons with the H_3^+ column densities from Fig. 3, and by using Fig. 5 to discount "high" water influx solutions, we can then derive a constraint on the maximum values for water influx and k_{fac} as a function of latitude. For example, in Fig. 4, there are many combinations of Φ_{H_2O} and k_{fac} that are capable of reproducing the $\sim 0.2 \times 10^{12}$ cm^{-2} H_3^+ column density derived from ring rain observations, but there are clear cutoffs in the maximum allowable water influx ($\sim 10^6$ cm^{-2} s^{-1}) and k_{fac} (~ 0.3) values.

3. Results

3.1. Maximum ring-derived water influx versus latitude

Results throughout the remainder of the text are based on simulations that explore 60 Φ_{H_2O} elements spread evenly in log space across 3×10^3–3×10^7 cm^{-2} s^{-1} and 60 k_{fac} elements spread evenly in log space across 0.003–3. Thus, there are 3600 individual model runs conducted for each of the 40 ring rain latitude elements. Both the Φ_{H_2O} and the k_{fac} ranges are chosen to capture the full range of possible maximum values for each parameter based on comparisons with H_3^+ column densities (Fig. 4).

Fig. 6 presents maximum ring-derived water influxes versus latitude, determined from model comparisons with the H_3^+ column densities shown in Fig. 3. The colored, dotted and dashed profiles correspond to those given Fig. 3, and therefore represent a range of possible upper limits on water influx, based on the various assumptions regarding H_3^+ temperatures at ring rain latitudes. In general, maximum water influxes are found to be larger in the southern hemisphere, while there are local maxima near 38° and 48° in the south and 42° and 53° in the north. The "instability region" described by O'Donoghue et al. (2013) maps to approximately 36–39° latitude in the south and 42–45° latitude in the north. This region lies between two "instability radii" located in the rings near $1.52R_S$ and $1.62R_S$, respectively. The former represents a stability limit for highly charged particles launched azimuthally in Saturn's ring plane at Keplerian circular velocity, while the latter represents a stability limit for particles in circular orbit (Northrop and Hill, 1982, 1983). At these radii outward centrifugal forces on charged particles are balanced by inward gravitational forces, leading to unstable regions in which particles can easily flow into Saturn's atmosphere along magnetic field lines.

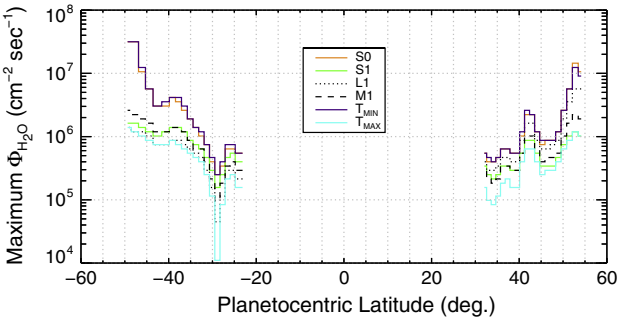

Fig. 6. Maximum ring rain water influx estimates versus latitude. A series of model simulations exploring a 60 × 60 grid of Φ_{H_2O} and k_{fac} values (see text) is used to find the maximum water influx that can reproduce the observed H_3^+ column densities derived in Fig. 3. Each profile represents the results from a different assumption regarding H_3^+ temperatures at ring rain latitudes (see Fig. 1).

Theory therefore predicts an enhancement of influx into Saturn's atmosphere at the latitudes on either side of the instability region. Though there remains significant scatter, on average Fig. 6 does have local maxima in the derived water influxes at the instability latitudes. The overall trend in water influx with latitude, however, differs from previous results (e.g., Moore et al., 2010), a fact discussed in more detail in Section 4.1.

Fig. 7 shows the maximum derived k_{fac} values versus latitude, based on model comparisons with the H_3^+ column densities derived in Fig. 3. Rather than showing the results of each of the six different assumptions made regarding ring rain temperatures (see Fig. 1), Fig. 7 is simplified and shows only results from the S1 fit (i.e., using the measurements from Smith et al., 1983; Koskinen et al., 2013; Vervack and Moses, submitted for publication). In addition, the mean hemispheric maximum k_{fac} values are also indicated by the dashed lines: 0.26 in the south and 0.17 in the north. Previous STIM comparisons with Cassini radio occultation measurements favored k_{fac} values of 0.075–0.25 (Moore et al., 2006) and 0.125 (Moore et al., 2010), a similar range to that derived in Fig. 7. Improved knowledge regarding the true values for k_{fac} present in Saturn's atmosphere could be used to refine the estimates for water influx. Rather than finding a maximum ring rain water influx for any value of k_{fac}, as in Fig. 6, we could find the model simulation that is best able to reproduce the observed H_3^+ column densities along a specified track of k_{fac} values. For example, if k_{fac} were fixed to 0.125, then the resulting best fit water influxes would be a factor of 2–3 smaller on average than the maximum values shown in Fig. 6. For k_{fac} = 0.25 the water influxes would be reduced by a factor of 10–12 on average.

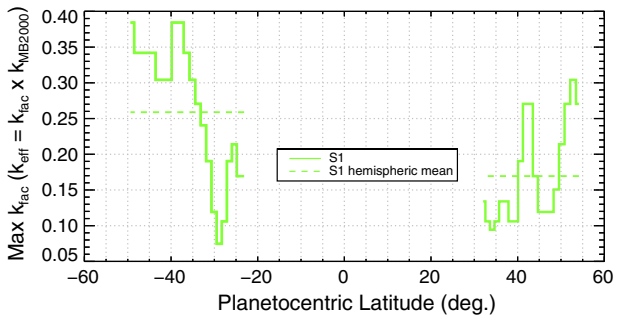

Fig. 7. Same as Fig. 6, but for k_{fac} values. Additionally, rather than show the k_{fac} values derived for each assumed H_3^+ temperature profile separately, we only show the k_{fac} values resulting from the green profile in Fig. 3 (solid line) along with the mean k_{fac} value for each hemisphere (dashed line). (For interpretation of the references to color in this figure legend, the reader is referred to the web version of this article.)

Based on UV spectra of Saturn obtained in 1994 with the Hubble Space Telescope (HST), Prangé et al. (2006) tentatively attributed an enhancement in the contrast in the 33°S planetocentric (R. Prangé, personal communication) latitude spectrum at 2000 Å and 1720 Å to a locally enhanced water abundance. While there is no obvious corresponding feature near 33°S latitude in Fig. 6, pointing uncertainties in the Prangé et al. measurements translate to an 8° uncertainty in latitude. Two local maxima in water influx derived in Fig. 6 are within this 8° latitude window, one near 26°S and one near 38°S. Prangé et al. also observed at $41^{\circ}{}^{+14^{\circ}}_{-11^{\circ}}$S and $52^{\circ}{}^{+35^{\circ}}_{-12^{\circ}}$S latitude, but were only able to place upper limits on water column density at those latitudes (of $<1.4 \times 10^{16}$ cm^{-2} and $<3.4 \times 10^{16}$ cm^{-2}, respectively). However, Prangé et al. noted that a local minimum in hydrocarbon abundance was present at 41°S, which could be interpreted as indirect evidence for a locally enhanced water influx, based on the modeling of Moses et al. (2000). Therefore, while there is no obvious direct correspondence between the possible detection of locally enhanced water abundance by Prangé et al. and by the latitudinal variations in water influx derived here, they share some consistent characteristics.

3.2. Global water influx and exogenous water sources

Water influxes derived here can be combined with previous results in order to estimate a global water influx. STIM comparisons with Cassini radio occultations were best able to reproduce the measured electron densities in Saturn's ionosphere when a latitudinally varying water influx was considered (Moore et al., 2010). Specifically, Moore et al. used a Gaussian water influx profile that peaked at Saturn's equator and had a variance σ of 10°. Fig. 8 shows this water profile (black, dashed line) along with the maximum water influxes from the green solid curve in Fig. 6, and with water influx estimates using a fixed k_{fac} of 0.125 and the S1 temperature fit (green, dotted line). The combined maximum water influx profile (i.e., solid + dashed curves) leads to an average water influx of 1.4×10^6 H_2O molecules cm^{-2} s^{-1} (averaged over the entire oblate Saturn spheroid) and a total global influx of 5.9×10^{26} H_2O molecules s^{-1}. This average influx is fairly close to the globally averaged value of $\sim 1.5 \times 10^6$ cm^{-2} s^{-1} derived by Moses et al. (2000) based on ISO observations (Feuchtgruber et al., 1997). While the variation with latitude shown in Fig. 8 is not strictly supported by Moses et al. (2000), as they found a best match to ISO observations using a constant influx versus latitude, it is not necessarily prohibited either. They only explored enhancements of 10^7 and 10^8 molecules cm^{-2} s^{-1}, above the range of the influxes calculated here. Therefore, it is possible that the less drastic variations in influx

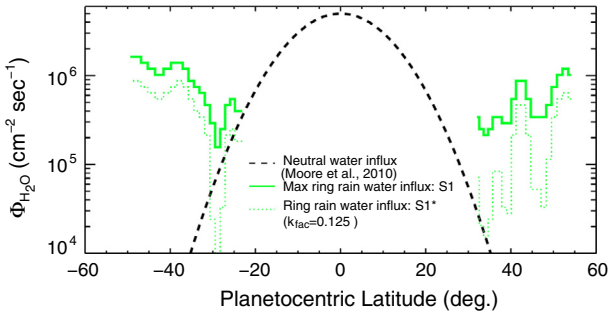

Fig. 8. Estimates of global water influxes based on the maximum water influxes calculated from ring rain observations (solid green profile, Fig. 6), water influxes estimated using a fixed k_{fac} of 0.125 and the S1 temperature fit (dotted green profile), and water influxes derived from model comparisons with Cassini radio occultation measurements (dashed black curve, Moore et al., 2010). (For interpretation of the references to color in this figure legend, the reader is referred to the web version of this article.)

with latitudinal shown in Fig. 8 are consistent with ISO observations.

Global water influx values given above are computed using the maximum water influxes shown in Fig. 8 (green solid profile). If k_{fac} is instead fixed to a specific value, such as 0.125 (e.g., Moore et al., 2010), then the resulting water influx values are reduced by a factor of 2–3 on average, yielding a globally averaged influx of 1.3×10^6 H_2O molecules cm^{-2} s^{-1} and a total global influx of 5.4×10^{26} s^{-1}. Different assumptions regarding temperatures at ring rain latitudes also affect the computed global influx values. Larger temperatures correspond to smaller H_3^+ densities (Fig. 3), which in turn reduce the water influx estimates (Fig. 6). The full range of globally averaged maximum water influxes, based on the temperature profiles of Fig. 1 and the resulting maximum water influxes of Fig. 6, is $(1.3–2.3) \times 10^6$ cm^{-2} s^{-1}. Similarly, the full range of total global maximum influx is $(5.6–10) \times 10^{26}$ s^{-1}. Note that the preceding values have been calculated by combining the dashed curve in Fig. 8 with model simulation results (Figs. 6 and 8). Results which omit the contribution from the dashed curve to the global mean influx – 1.1×10^6 cm^{-2} s^{-1} and 4.9×10^{26} s^{-1}, respectively – are summarized in Table 1.

While we cannot explicitly identify the source of exogenous water based on the modeling, the derived water influx rates can be further broken into a "neutral" source (Moore et al., 2010) and a "ring rain" ionized source (this work). The total global influx of 5.9×10^{26} s^{-1} given above then represents the sum of a neutral source of 4.9×10^{26} s^{-1} and a ring rain source of 1.0×10^{26} s^{-1} (S1 temperature fit). Assuming the "neutral" source originates from Enceladus with a rate of 10^{28} s^{-1} (Jurac and Richardson, 2007; Cassidy and Johnson, 2010), our derived neutral influx represents ~5% of the water ejected from Enceladus' plumes, within a factor of two of current model predictions for Enceladus oxygen products lost to Saturn's atmosphere: 10%, 7%, 3%, and 6%, respectively (Jurac and Richardson, 2007; Cassidy and Johnson, 2010; Hartogh et al., 2011; Fleshman et al., 2012). Similarly, if the assumed "ring rain" source is entirely from the rings, then it represents about 10% of the $\sim 10^{27}$ s^{-1} ions produced in Saturn's ring atmosphere (Johnson et al., 2006), and the globally averaged maximum ring-derived water influx of 2.4×10^5 cm^{-2} s^{-1} is in rough agreement with the total oxygen influx of $\sim 10^5$ cm^{-2} s^{-1} estimated from ring atmosphere models (e.g., Tseng et al., 2010). Furthermore, as first predicted by Connerney (1986), precipitation is expected to be enhanced at southern latitudes due to Saturn's effectively offset magnetic dipole (Burton et al., 2010), independent of Saturn season (e.g., Northrop and Connerney, 1987; Luhmann et al., 2006; Tseng et al., 2010). This enhancement is also present here, though the magnitude is weaker than predicted by a factor of ~5. For example, the mean water influx for $k_{fac} = 0.125$ model results is 4.5×10^5 cm^{-2} s^{-1} in the southern hemisphere and 2.0×10^5 cm^{-2} s^{-1} in the northern hemisphere (S1* temperature fit; green dotted profile in Fig. 8). Taken together, these comparisons provide evidence that the oxygen influx at Saturn can be quantitatively attributed to two separate sources: Saturn's rings and Enceladus. Further sources, such as interplanetary dust particles and cometary impacts, remain possible, though are likely not required to explain current observations of Saturn's upper atmosphere.

3.3. Ring mass loss rates and lifetime estimate

In order to estimate the ring mass loss implied by water influxes calculated in this work, we first convert the variations of influx in latitude to variations in radius in Saturn's ring plane. We use the axisymmetric magnetic mapping model of Bunce et al. (2008) with updated internal field coefficients based on Cassini measurements (Burton et al., 2010). We set the height of the ionosphere to 1100 km above the 1-bar level, where the peak H_3^+ density is approximately located (Stallard et al., 2012), and use the IAU Saturn equatorial radius value of 60,268 km (Seidelmann et al., 2007). Further details and magnetic mapping model comparisons are given in the O'Donoghue et al. (2013) supplementary information.

Fig. 9 shows the result of mapping the ring rain water influxes of Fig. 8 along magnetic field lines into Saturn's equatorial plane. In order to give some sense of ring structure, we also plot ring normal optical depths measured in the IR from ground based occultations of 28 Sgr (Nicholson et al., 2000). Two points are immediately evident from the figure. First, there is a local maximum of ring rain influx at $\sim 1.52 R_S$, near the edge of the instability radius, consistent with predictions (e.g., Northrop and Hill, 1983). Second, the north–south asymmetry in derived water influxes is even more obvious when plotted together; the southern water fluxes dominate all of the equatorial structure. This last point further strengthens the prediction from ring atmosphere models that the southern ring atmosphere (and resulting precipitation into Saturn's atmosphere) is always stronger than the northern ring atmosphere due to the effectively offset magnetic dipole (e.g., Connerney, 1986; Northrop and Connerney, 1987; Tseng et al., 2010), as the sub-solar point during ring rain observations was +9.1°, and therefore the Sun primarily illuminated the northern ring face.

It is difficult to make accurate measurements of the total mass of Saturn's rings, as the standard assumption of uniform distribution of ring particles neglects the possibility of particles clumping into large gravitational aggregates, and therefore previous determinations likely represent only lower bounds on ring mass. Similarly, while we express ring derived precipitation influxes as "water" in this work, they could be equally well represented by heavier oxygen compounds and/or dust grains. Therefore, an estimate of ring mass loss based on the assumption of H_2O influx is a lower limit. Nevertheless, it is worthwhile to assess the possible impact of our calculated influxes on ring evolution.

Table 1
Estimated water influxes from model simulation comparisons with derived ring rain H_3^+ column densities.

Temperature fit ID	Fit type	Data used[a]	Globally averaged "Ring rain" influx ($\times 10^6$ cm^{-2} s^{-1})	Total "ring rain" influx ($\times 10^{26}$ s^{-1})
Maximum water influx estimate method				
S0	Sinusoidal	[1], [5]	1.2	5.1
S1	Sinusoidal	[1], [5], [6]	0.24	1.0
L1	Linear	[1], [5], [6]	0.31	1.4
M1	Mean	[1], [5], [6]	0.28	1.2
T_{MIN}	T_{exo} minimum	–	1.2	5.2
T_{MAX}	T_{exo} maximum	–	0.16	6.8
Fixed k_{fac} water influx estimate method				
S1*	Sinusoidal; $k_{fac} = 0.125$	[1], [5], [6]	0.11	0.49
S1**	Sinusoidal; $k_{fac} = 0.25$	[1], [5], [6]	0.04	0.17

[a] [1] Smith et al. (1983); [5] Vervack and Moses (submitted for publication); [6] Koskinen et al. (2013).

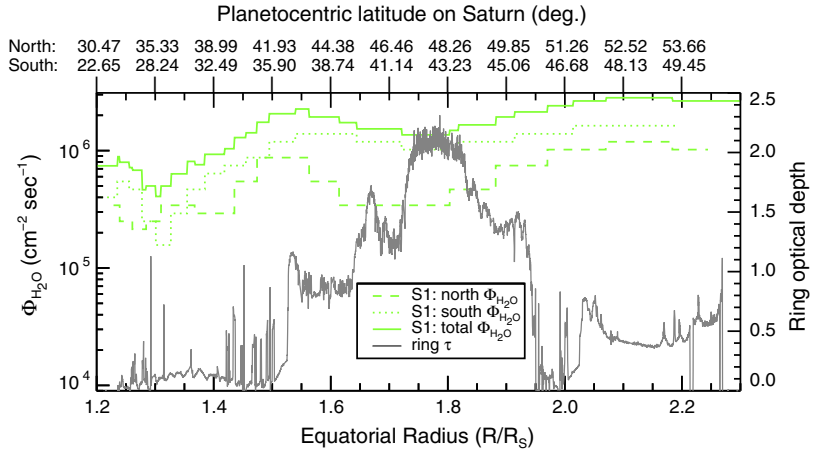

Fig. 9. Maximum water influx estimates, based on H_3^+ column densities derived from ring rain observations (Fig. 3), and model comparisons. The influxes from Fig. 8 are mapped along magnetic field lines to Saturn's ring plane (see text). Northern hemisphere water influxes (dashed green line) and southern hemisphere influxes (dotted green line) are shown as well as a combined hemispheric influx (solid green line). In addition, ring normal optical depths from IR ground based stellar occultation observations are plotted in gray. (For interpretation of the references to color in this figure legend, the reader is referred to the web version of this article.)

Using Voyager measurements, Esposito et al. (1983) calculated a total ring mass of 2.8×10^{19} kg, roughly distributed as 6.25×10^{18} kg in the A ring, 1.93×10^{19} kg in the B ring, and 7.96×10^{17} kg in the C ring. Later estimates include $(4–7) \times 10^{19}$ kg for the B ring (Robbins et al., 2010), as well as 4.9×10^{18} kg and $(5–7) \times 10^{18}$ kg for the A ring (Spilker et al., 2004; Robbins et al., 2010). Converting integrated water influxes derived in Section 3.1. (Fig. 9) to implied mass loss rates gives 10 kg s^{-1} for the A ring, 8.8 kg s^{-1} for the B ring, and 2.7 kg s^{-1} for the C ring. This calculation assumes a pure water influx in order to convert the Fig. 9 values to mass influx, and then integrates the derived mass influxes over the ring regions defined in Table II of Esposito et al. (1983). If we use those mass loss rates and the Esposito et al. (1983) ring mass estimates, and we make the (likely unrealistic) assumption that they hold constant in time (with no other source replenishing the rings), then the maximum lifetimes of the A, B and C rings are ~20, ~70, and ~9.3 byr, respectively. However, in addition to only representing an upper limit, the impact of these lifetimes is further reduced by their reliance on a number of key assumptions, which include a constant ring rain loss rate, and their neglect of the possibility of narrow regions of enhanced ring loss (as such signatures would have been smoothed out due to the latitude resolution of the ring rain observations). More thorough estimates of ring lifetimes, using varying techniques, include 4.4–67 myr (Northrop and Connerney, 1987), 100 myr (Cuzzi and Estrada, 1998; Salmon et al., 2010), and 4.5 byr (Canup, 2010). An overview of many past ring evolution studies is given by Chambers et al. (2008).

4. Discussion and conclusion

Quantifying the magnitude and temporal and spatial variability of the observed exogenous source(s) of oxygen at Saturn is important for atmospheric chemistry and physics. Dust particles can lead to localized heating of the upper atmosphere, thereby affecting atmospheric dynamics (e.g., Rizk and Hunten, 1990), they can alter atmospheric photochemistry through attenuation of solar UV radiation, and they can facilitate stratospheric haze formation by providing condensation nuclei in the upper atmosphere (e.g., Moses et al., 2000, and references therein). Similarly, vapor species can significantly alter stratospheric and ionospheric chemistry (Connerney and Waite, 1984; Majeed and McConnell, 1991; Moses et al., 2000).

Indirect estimates of oxygen influx at Saturn use a measurement of one or more other atmospheric parameters – typically electron density – in order to reproduce the observed parameter(s). Previous indirect estimates include fluxes of 10^7 OH cm^{-2} s^{-1} (Shimizu, 1980), $\sim 10^{10}$ OH cm^{-2} s^{-1} (Chen, 1983), $\sim 4 \times 10^7$ H_2O cm^{-2} s^{-1} (Connerney and Waite, 1984), 2.2×10^7 H_2O cm^{-2} s^{-1} (Majeed and McConnell, 1991), $(1–5) \times 10^7$ cm^{-2} s^{-1} (Majeed and McConnell, 1996), and 5×10^6 H_2O cm^{-2} s^{-1} (Moore et al., 2006). These estimates are all based on one or more radio occultation measurements, or on Saturn Electrostatic Discharge (SED) observations, and represent local influxes for the most part, as the observations are relatively sparse. Radio occultations sample Saturn's dawn or dusk ionosphere at one point in time and therefore provide little opportunity for constraining the possible temporal or spatial variation of the derived influx. In contrast, SEDs use the low frequency cutoff from radio emissions generated by lightning in Saturn's lower atmosphere to derive local time variations in peak ionospheric electron density. SED measurements exist for both the Voyager (Kaiser et al., 1984) and Cassini (Fischer et al., 2011) eras, and indicate strong diurnal variations in electron density that models have not yet been able to explain (Majeed and McConnell, 1996; Moore et al., 2012).

The primary difficulty faced by previous model comparisons with SED-derived diurnal variations in peak electron density is the extremely rapid buildup of ionization in the morning hours implied by the measurements. For example, the net (i.e., production minus loss) electron production rate between dawn and noon from SED measurements is between ~9 cm^{-3} s^{-1} (Cassini; Fischer et al., 2011) and ~30–70 cm^{-3} s^{-1} (Voyager; Kaiser et al., 1984; Zarka, 1985), whereas the peak overhead production rate due to solar EUV is ~10 cm^{-3} s^{-1} (Moore et al., 2004). Therefore, an explanation of SED observations may require some sort of extreme ionization enhancement process, such as due to a diurnal ionosphere–protonosphere exchange (e.g. Connerney and Waite, 1984). One alternative explanation is that SEDs may be sampling the sharp low-altitude ionospheric layers frequently seen in radio occultation electron density profiles (Nagy et al., 2006; Kliore et al., 2009) rather than the canonical ionospheric peak. Such layers are consistent with the presence of gravity waves in Saturn's lower thermosphere (Matcheva and Barrow, 2012), and can lead to narrow regions of electron density enhancements without requiring any additional sources of ionization (Barrow and Matcheva, 2013). As the atmospheric storms that give rise to SEDs tend to occur only at a limited set of specific latitudes for currently

unknown reasons (primarily 35°S; Fischer et al., 2011), any ionospheric explanation of SED-derived electron densities may also be local in nature.

Direct measurements of oxygen species in Saturn's upper atmosphere have proven difficult. The first unambiguous direct detection of water in Saturn's upper atmosphere came from the ISO (Feuchtgruber et al., 1997), which led to a derivation of global water influx of $\sim 1.5 \times 10^6$ H_2O molecules cm^{-2} s^{-1} (Moses et al., 2000), similar to later SWAS and Herschel values (Bergin et al., 2000; Hartogh et al., 2011). Two ambiguous detections have been made in the UV, one by the International Ultraviolet Explorer satellite (Winkelstein et al., 1983), and one by HST, which indicated possible locally enhanced water abundance near 33°S latitude (Prangé et al., 2006). Cassini's Composite Infrared Spectrometer (CIRS) instrument has also detected weak H_2O emission lines, which should allow a retrieval of latitudinal variation of water at Saturn in the future (Bjoraker et al., 2010), with a preliminary analysis indicating a qualitatively similar latitudinal trend to that derived by Moore et al. (2010).

Observations of H_3^+ allow for a significantly improved indirect estimate of external oxygen influx at Saturn, as they can provide an extended latitude distribution of H_3^+ column densities in a single snapshot. Though uncertainty in some Saturn ionospheric photochemical reactions remains, such as the effective rate of charge exchange between H^+ and vibrationally excited H_2, the water influxes derived here agree well with a number of different studies. They represent a global influx that is comparable to the expected water vapor loss from Enceladus to Saturn's atmosphere (Jurac and Richardson, 2007; Cassidy and Johnson, 2010; Hartogh et al., 2011; Fleshman et al., 2012), and a ring derived influx with a magnitude and hemispheric asymmetry consistent with earlier predictions (e.g., Connerney, 1986) and ring atmosphere calculations (Luhmann et al., 2006; Tseng et al., 2010). Local peak influxes are at latitudes that map magnetically to instability radii in Saturn's rings, long predicted to be a prime location for siphoning material from Saturn's rings into its atmosphere (e.g., Northrop and Hill, 1982, 1983; Connerney, 1986). The latitudinally averaged influx is in good agreement with that derived from ISO measurements (Feuchtgruber et al., 1997), while the latitudinal variations in influx are likely not drastic enough to conflict with the constraints derived by Moses et al. (2000).

Taken together, the above agreements with previous work demonstrate an internal consistency which makes the derived values more convincing. However, there are also a number of limitations to the current approach. These include: a lack of self-consistent H_3^+ temperatures from the ring rain observations, an insufficient latitude resolution for direct comparisons with predicted narrow regions of enhanced ring-derived influx (e.g., Connerney and Waite, 1984; Connerney, 1986), and an assumption of constant influx. For example, electron column contents from radio occultation observations are used to discount solutions with large water influxes (e.g., $>10^7$ cm^{-2} s^{-1}; Fig. 5). However, if the external water influx at Saturn is time-variable (e.g., Moore and Mendillo, 2007), as opposed to constant as considered here, then this argument would be weakened, as the radio occultations of electron densities and the H_3^+ observations were taken years apart and sample different local times. Furthermore, radio occultations sample a range of latitudes while relying on the assumption of a horizontally stratified ionosphere, and consequently would not be expected to detect narrowly confined ionospheric perturbations, such as from a region of enhanced water influx. Therefore, despite the discrepancy between model results and measured column electron densities for large water influxes shown in Fig. 5, the "high" water influx family of solutions shown in Fig. 4 cannot be dismissed unequivocally without further observational evidence.

4.1. Radio occultation observations

There is a discrepancy between the latitudinal variation of water influxes calculated here and that derived based on comparisons with Cassini radio occultation measurements (Fig. 8; also Moore et al., 2010). In fact, the ring rain water influxes from this work lead to a mid-latitude trend in electron density – a decrease with increasing latitude – that is counter to what has been observed (Kliore et al., 2009). There are a number of possible explanations for this fact. First, while the observed neutral temperatures seem to increase with latitude, the STIM-derived temperature differentials also increase with latitude (Fig. 2). This leads to a prediction for H_3^+ temperatures that is flat or decreasing with latitude, and an inverse trend in H_3^+ column densities. Consequently, the resulting water influx estimates also increase with latitude. Future ring rain observations should be able to address this possibility, as the O'Donoghue et al. (2013) results were based on only ~2 h of data; longer integrations will allow for self-consistent H_3^+ temperature and density measurements. Second, there are only 5 published Cassini radio occultations within the ring rain latitudes, whereas 31 radio occultations were used to derive the latitudinal trend in electron density. This means that the overall trend was anchored by the 18 equatorial radio occultation profiles and increased with latitude to match the 8 high-latitude profiles. Further mid-latitude Cassini radio occultations will help to establish the strength of the latitudinal electron density trend there, and may reveal localized minima and maxima with the increased latitude resolution, if present. Finally, the Cassini radio occultations occurred 3–6 years prior to the ring rain observations (and thus to a different season and solar cycle phase), and so it may not be reasonable to expect that one set of parameters should reproduce both data sets simultaneously.

4.2. Summary

Based on model comparisons with observations of mid- and low-latitude H_3^+ emission at Saturn, detected recently for the first time, we have estimated maximum ring-derived water influxes as a function of latitude on the planet and as a function of radius in the ring plane. We find globally averaged maximum ring-derived water influxes of $(1.6–12) \times 10^5$ cm^{-2} s^{-1}, which corresponds to a maximum total global rate of water molecules from Saturn's rings to its atmosphere of $(1.0–6.8) \times 10^{26}$ s^{-1}. Though they represent a non-unique solution, our distribution of influxes is in good agreement with a range of predictions resulting from different aspects of Saturn system science. Future observations of mid-latitude H_3^+ at Saturn would allow for significant improvements to this work, including: (1) an increased latitude resolution (as Saturn tilts more toward Earth in its approach to northern summer solstice); (2) an examination of any seasonal or temporal differences; and (3) a self-consistent measurement of H_3^+ temperature. This last point is extremely important, because the necessary fundamental assumption in this study is that the observed structure in H_3^+ emission is caused by variations in H_3^+ column density (driven by a water influx), and not by variations in H_3^+ temperatures. Determination of the external oxygen influx at Saturn is relevant for a wide range of atmospheric chemistry and dynamics. As the timescale for diffusion through the upper atmosphere is rapid compared to the lower atmosphere, observing the upper atmospheric signatures of such an influx is key for gauging its spatial and temporal variability.

Acknowledgments

We acknowledge the contribution of the International Space Sciences Institute (ISSI) in Bern, Switzerland, for hosting and

funding the ISSI International Team on "Comparative Jovian Aeronomy", and the constructive discussions by colleagues attending the meetings. Funding for this work at Boston University comes from NASA Grants NNX13AG21G and NNX13AG57G. J.O'D. was supported by the UK Science and Technology Facilities Council (STFC) through a PhD Studentship. I.M.W. and M.G. were partially funded by STFC through the Consolidated Grant to Imperial College London.

References

Bergin, E.A. et al., 2000. Submillimeter wave astronomy satellite observations of Jupiter and Saturn: detection of 557 GHz water emission from the upper atmosphere. Astrophys. J. 4 (539), 147–150.

Bjoraker, G., Achterberg, R.K., Jennings, D.E., 2010. Cassini/CIRS observations of water vapor in Saturn's stratosphere. In: EPSC Abstracts, vol. 5, p. 9007.

Broadfoot, A.L. et al., 1981. Extreme ultraviolet observations from Voyager 1 encounter with Saturn. Science 212 (4491), 206–211.

Bunce, E.J., Arridge, C.S., Cowley, S.W.H., Dougherty, M.K., 2008. Magnetic field structure of Saturn's dayside magnetosphere and its mapping to the ionosphere: Results from ring current modeling. J. Geophys. Res. 113 (A2), A02207. http://dx.doi.org/10.1029/2007JA012538.

Burton, M.E., Dougherty, M.K., Russell, C.T., 2010. Saturn's internal planetary magnetic field. Geophys. Res. Lett. 37 (24). http://dx.doi.org/10.1029/2010GL045148, n/a–n/a.

Canup, R.M., 2010. Origin of Saturn's rings and inner moons by mass removal from a lost Titan-sized satellite. Nature 468 (7326), 943–946. http://dx.doi.org/10.1038/nature09661.

Capone, L.A., Whitten, R.C., Prasad, S.S., Dubach, J., 1977. The ionospheres of Saturn, Uranus, and Neptune. Astrophys. J. 215, 977–983.

Cassidy, T.A., Johnson, R.E., 2010. Collisional spreading of Enceladus' neutral cloud. Icarus 209 (2), 696–703. http://dx.doi.org/10.1016/j.icarus.2010.04.010.

Chambers, L.S., Cuzzi, J.N., Asphaug, E., Colwell, J., Sugita, S., 2008. Hydrodynamical and radiative transfer modeling of meteoroid impacts into Saturn's rings. Icarus 194 (2), 623–635. http://dx.doi.org/10.1016/j.icarus.2007.11.017.

Chen, R.H., 1983. Saturn's ionosphere: A corona of ice particles? Moon Planets 28, 37–41.

Connerney, J.E.P., 1986. Magnetic connection for Saturn's rings and atmosphere. Geophys. Res. Lett. 13 (8), 773–776.

Connerney, J., 2013. Saturn's ring rain. Nature 496 (7444), 178–179.

Connerney, J., Waite, J., 1984. New model of Saturn's ionosphere with an influx of water from the rings. Nature 312, 136–138.

Cravens, T.E., 1987. Vibrationally excited molecular hydrogen in the upper atmosphere of Jupiter. J. Geophys. Res. 92 (5), 11083–11100.

Cuzzi, J.N., Estrada, P.R., 1998. Compositional evolution of Saturn's rings due to meteoroid bombardment. Icarus 132, 1–35.

Cuzzi, J.N. et al., 2010. An evolving view of Saturn's dynamic rings. Science 327 (5972), 1470–1475. http://dx.doi.org/10.1126/science.1179118.

Esposito, L.W., O'Callaghan, M., West, R.A., 1983. The structure of Saturn's rings: Implications from the Voyager stellar occultation. Icarus 56 (3), 439–452. http://dx.doi.org/10.1016/0019-1035(83)90165-3.

Festou, M.C., Atreya, S.K., 1982. Voyager ultraviolet stellar occultation measurements of the composition and thermal profiles of the saturnian upper atmosphere. Geophys. Res. Lett. 9 (10), 1147–1150.

Feuchtgruber, H., Lellouch, E., De Graauw, T., 1997. External supply of oxygen to the atmospheres of the giant planets. Nature 389 (September), 159–162.

Fischer, G., Gurnett, D.a., Zarka, P., Moore, L., Dyudina, U.A., 2011. Peak electron densities in Saturn's ionosphere derived from the low-frequency cutoff of Saturn lightning. J. Geophys. Res. 116 (A4), A04315. http://dx.doi.org/10.1029/2010JA016187.

Fleshman, B.L., Delamere, P.A., Bagenal, F., Cassidy, T., 2012. The roles of charge exchange and dissociation in spreading Saturn's neutral clouds. J. Geophys. Res. 117 (E5), E05007. http://dx.doi.org/10.1029/2011JE003996.

French, R., Nicholson, P.D., 2000. Saturn's rings II particle sizes inferred from stellar occultation data. Icarus 145 (2), 502–523. http://dx.doi.org/10.1006/icar.2000.6357.

Gérard, J.-C. et al., 2009. Altitude of Saturn's aurora and its implications for the characteristic energy of precipitated electrons. Geophys. Res. Lett. 36 (2). http://dx.doi.org/10.1029/2008GL036554, n/a–n/a.

Hartogh, P. et al., 2011. Direct detection of the Enceladus water torus with Herschel. Astron. Astrophys. 532, L2. http://dx.doi.org/10.1051/0004-6361/201117377.

Hubbard, W.B. et al., 1997. Structure of Saturn's mesosphere from the 28 Sgr occultations. Icarus 130, 404–425.

Huestis, D.L., 2008. Hydrogen collisions in planetary atmospheres, ionospheres, and magnetospheres. Planet. Space Sci. 56 (13), 1733–1743. http://dx.doi.org/10.1016/j.pss.2008.07.012.

Huestis, D.L. et al., 2008. Cross sections and reaction rates for comparative planetary aeronomy. Space Sci. Rev. 139 (1–4), 63–105. http://dx.doi.org/10.1007/s11214-008-9383-7.

Johnson, R.E. et al., 2006. Production, ionization and redistribution of O_2 in Saturn's ring atmosphere. Icarus 180 (2), 393–402. http://dx.doi.org/10.1016/j.icarus.2005.08.021.

Jurac, S., Richardson, J.D., 2007. Neutral cloud interaction with Saturn's main rings. Geophys. Res. Lett. 34 (8), L08102. http://dx.doi.org/10.1029/2007GL029567.

Kaiser, M.L., Desch, M.D., Connerney, J.E.P., 1984. Saturn's ionosphere: Inferred electron densities. J. Geophys. Res. 89 (A4), 2371. http://dx.doi.org/10.1029/JA089iA04p02371.

Kliore, A.J., Patel, I.R., Lindal, G.F., Sweetnam, D.N., Hotz, H.B., 1980. Structure of the ionosphere and atmosphere of Saturn from Pioneer 11 Saturn radio occultation. J. Geophys. Res. 85 (A11), 5857–5870.

Kliore, A.J. et al., 2009. Midlatitude and high-latitude electron density profiles in the ionosphere of Saturn obtained by Cassini radio occultation observations. J. Geophys. Res. 114 (A4), A04315. http://dx.doi.org/10.1029/2008JA013900.

Koskinen, T.T., Sandel, B.R., Yelle, R.V., Capalbo, F.J., Holsclaw, G.M., McClintock, W.E., Edgington, S., 2013. The density and temperature structure near the exobase of Saturn from Cassini UVIS solar occultations. Icarus 226 (2), 1318–1330. http://dx.doi.org/10.1016/j.icarus.2013.07.037.

Lindal, G.F., Sweetnam, D.N., Eshleman, V.R., 1985. The atmosphere of Saturn: An analysis of the Voyager radio occultation measurements. Astron. J. 90 (6), 1136–1146.

Luhmann, J.G., Johnson, R.E., Tokar, R.L., Ledvina, S.a., Cravens, T.E., 2006. A model of the ionosphere of Saturn's rings and its implications. Icarus 181 (2), 465–474. http://dx.doi.org/10.1016/j.icarus.2005.11.022.

Majeed, T., McConnell, J., 1991. The upper ionospheres of Jupiter and Saturn. Planet. Space Sci. 39 (12), 1715–1732.

Majeed, T., McConnell, J., 1996. Voyager electron density measurements on Saturn: Analysis with a time dependent ionospheric model. J. Geophys. Res. 101, 7589–7598.

Majeed, T., McConnell, J., Yelle, R., 1990. Vibrationally excited H_2 in the upper atmosphere of Saturn. Adv. Space Res. 10 (1), 131–134.

Majeed, T., McConnell, J., Yelle, R., 1991. Vibrationally excited H_2 in the outer planets thermosphere: Fluorescence in the Lyman and Werner bands. Planet. Space Sci. 39 (11), 1591–1606.

Matcheva, K.I., Barrow, D.J., 2012. Small-scale variability in Saturn's lower ionosphere. Icarus 221 (2), 525–543. http://dx.doi.org/10.1016/j.icarus.2012.08.022.

McElroy, M., 1973. The ionospheres of the major planets. Space Sci. Rev. 14, 460–473.

Melin, H., Miller, S., Stallard, T., Trafton, L.M., Geballe, T.R., 2007. Variability in the H_3^+ emission of Saturn: Consequences for ionisation rates and temperature. Icarus 186 (1), 234–241. http://dx.doi.org/10.1016/j.icarus.2006.08.014.

Melin, H. et al., 2011. Simultaneous Cassini VIMS and UVIS observations of Saturn's southern aurora: Comparing emissions from H, H_2 and H_3^+ at a high spatial resolution. Geophys. Res. Lett. 38 (15). http://dx.doi.org/10.1029/2011GL048457, n/a–n/a.

Miller, S., Joseph, R.D., Tennyson, J., 1990. Infrared emissions of H_3^+ in the atmosphere of Jupiter in the 2.1 and 4.0 micron region. Astrophys. J. 360, L55–L58.

Miller, S. et al., 2000. The role of H_3^+ in planetary atmospheres. Philos. Trans. R. Soc. A: Math. Phys. Eng. Sci. 358, 2485–2502.

Miller, S., Stallard, T., Melin, H., Tennyson, J., 2010. H_3^+ cooling in planetary atmospheres. Faraday Discuss. 147, 283. http://dx.doi.org/10.1039/c004152c.

Moore, L., Mendillo, M., 2007. Are plasma depletions in Saturn's ionosphere a signature of time-dependent water input? Geophys. Res. Lett. 34 (12), L12202. http://dx.doi.org/10.1029/2007GL029381.

Moore, L.E., Mendillo, M., Müller-Wodarg, I.C.F., Murr, D.L., 2004. Modeling of global variations and ring shadowing in Saturn's ionosphere. Icarus 172 (2), 503–520. http://dx.doi.org/10.1016/j.icarus.2004.07.007.

Moore, L., Nagy, A.F., Kliore, A.J., Müller-Wodarg, I., Richardson, J.D., Mendillo, M., 2006. Cassini radio occultations of Saturn's ionosphere: Model comparisons using a constant water flux. Geophys. Res. Lett. 33 (22), L22202. http://dx.doi.org/10.1029/2006GL027375.

Moore, L., Galand, M., Mueller-Wodarg, I., Yelle, R., Mendillo, M., 2008. Plasma temperatures in Saturn's ionosphere. J. Geophys. Res. 113 (A10), A10306. http://dx.doi.org/10.1029/2008JA013373.

Moore, L., Galand, M., Mueller-Wodarg, I., Mendillo, M., 2009. Response of Saturn's ionosphere to solar radiation: Testing parameterizations for thermal electron heating and secondary ionization processes. Planet. Space Sci. 57 (14–15), 1699–1705. http://dx.doi.org/10.1016/j.pss.2009.05.001.

Moore, L., Mueller-Wodarg, I., Galand, M., Kliore, A., Mendillo, M., 2010. Latitudinal variations in Saturn's ionosphere: Cassini measurements and model comparisons. J. Geophys. Res. 115 (A11), A11317. http://dx.doi.org/10.1029/2010JA015692.

Moore, L., Fischer, G., Müller-Wodarg, I., Galand, M., Mendillo, M., 2012. Diurnal variation of electron density in Saturn's ionosphere: Model comparisons with Saturn Electrostatic Discharge (SED) observations. Icarus 221 (2), 508–516. http://dx.doi.org/10.1016/j.icarus.2012.08.010.

Moses, J., Bass, S., 2000. The effects of external material on the chemistry and structure of Saturn's ionosphere. J. Geophys. Res. 105 (1999), 7013–7052.

Moses, J., Bézard, B., Lellouch, E., Gladstone, G.R., Feuchtgruber, H., Allen, M., 2000. Photochemistry of Saturn's atmosphere II. Effects of an influx of external oxygen. Icarus 145 (1), 166–202. http://dx.doi.org/10.1006/icar.1999.6320.

Müller-Wodarg, I.C.F., Moore, L., Galand, M., Miller, S., Mendillo, M., 2012. Magnetosphere–atmosphere coupling at Saturn: 1 – Response of thermosphere and ionosphere to steady state polar forcing. Icarus 221 (2), 481–494. http://dx.doi.org/10.1016/j.icarus.2012.08.034.

Nagy, A.F. et al., 2006. First results from the ionospheric radio occultations of Saturn by the Cassini spacecraft. J. Geophys. Res. 111 (A6), A06310. http://dx.doi.org/10.1029/2005JA011519.
Neale, L., Miller, S., Tennyson, J., 1996. Spectroscopic properties of the H_3^+ molecule: A new calculated line list. Astrophys. J. 464, 516–520.
Nicholson, P., French, R., Tollestrup, E., Cuzzi, J., Harrington, J., Matthews, K., Perkovic, O., Stover, R., 2000. Saturn's rings I optical depth profiles from the 28 Sgr occultation. Icarus 145 (2), 474–501. http://dx.doi.org/10.1006/icar.2000.6356.
Northrop, T.G., Connerney, J.E.P., 1987. A micrometeorite erosion model and the age of Saturn's rings. Icarus 70, 124–137.
Northrop, G., Hill, J.R., 1982. Stability of negatively charged dust Graings in Saturn's ring plane. J. Geophys. Res. 87 (A8), 6045–6051.
Northrop, T.G., Hill, J.R., 1983. The inner edge of Saturn's B ring. J. Geophys. Res. 88 (A8), 6102–6108.
O'Donoghue, J. et al., 2013. The domination of Saturn's low-latitude ionosphere by ring "rain". Nature 496 (7444), 193–195. http://dx.doi.org/10.1038/nature12049.
O'Donoghue, J., Stallard, T.S., Melin, H., Cowley, S.W.H., Badman, S.V., Moore, L., Miller, S., Tao, C., Baines, K.H., Blake, J.S.D., 2014. Conjugate observations of Saturn's northern and southern aurorae. Icarus 229, 214–220. http://dx.doi.org/10.1016/j.icarus.2013.11.009.
Barrow, D.J., Matcheva, K.I., 2013. Modeling the effect of atmospheric gravity waves on Saturn's ionosphere. Icarus 224 (1), 32–42. http://dx.doi.org/10.1016/j.icarus.2013.01.027.
Prangé, R., Fouchet, T., Courtin, R., Connerney, J.E.P., McConnell, J.C., 2006. Latitudinal variation of Saturn photochemistry deduced from spatially-resolved ultraviolet spectra. Icarus 180 (2), 379–392. http://dx.doi.org/10.1016/j.icarus.2005.11.005.
Rizk, B., Hunten, D.M., 1990. Solar heating of the uranian mesopause by dust of ring origin. Icarus 88 (2), 429–447. http://dx.doi.org/10.1016/0019-1035(90)90093-O.
Robbins, S.J., Stewart, G.R., Lewis, M.C., Colwell, J.E., Sremčević, M., 2010. Estimating the masses of Saturn's A and B rings from high-optical depth N-body simulations and stellar occultations. Icarus 206 (2), 431–445. http://dx.doi.org/10.1016/j.icarus.2009.09.012.
Salmon, J., Charnoz, S., Crida, a., Brahic, a., 2010. Long-term and large-scale viscous evolution of dense planetary rings. Icarus 209 (2), 771–785. http://dx.doi.org/10.1016/j.icarus.2010.05.030.
Sandel, A.B.R. et al., 1982. Extreme ultraviolet observations from the Voyager 2 encounter with Saturn. Science 215 (4532), 548–553.
Seidelmann, P.K. et al., 2007. Report of the IAU/IAG working group on cartographic coordinates and rotational elements: 2006. Celest. Mech. Dynam. Astron. 98 (3), 155–180. http://dx.doi.org/10.1007/s10569-007-9072-y.
Shemansky, D.E., Liu, X., 2012. Saturn upper atmospheric structure from Cassini EUV and FUV occultations. Can. J. Phys. 90 (8), 817–831. http://dx.doi.org/10.1139/p2012-036.
Shimizu, M., 1980. Strong interaction between the ring system and the ionosphere of Saturn. Moon Planets 22, 521–522.
Smith, G.R., Shemansky, D.E., Holberg, J.B., Broadfoot, A.L., Sandel, B.R., 1983. Saturn's upper atmosphere from the Voyager 2 EUV solar and stellar occultations. J. Geophys. Res. 88 (A11), 8667–8678.
Spilker, L.J., Pilorz, S., Lane, A.L., Nelson, R.M., Pollard, B., Russell, C.T., 2004. Saturn A ring surface mass densities from spiral density wave dispersion behavior. Icarus 171 (2), 372–390. http://dx.doi.org/10.1016/j.icarus.2004.05.016.
Stallard, T., Miller, S., Millward, G., Joseph, R.D., 2002. On the dynamics of the Jovian ionosphere and thermosphere II. The measurement of H_3^+ vibrational temperature, column density, and total emission. Icarus 156 (2), 498–514. http://dx.doi.org/10.1006/icar.2001.6793.
Stallard, T.S., Melin, H., Miller, S., Badman, S.V., Brown, R.H., Baines, K.H., 2012. Peak emission altitude of Saturn's H_3^+ aurora. Geophys. Res. Lett. 39 (15), 1–5. http://dx.doi.org/10.1029/2012GL052806.
Tokar, R.L. et al., 2005. Cassini observations of the thermal plasma in the vicinity of Saturn's main rings and the F and G rings. Geophys. Res. Lett. 32 (14), 1–5. http://dx.doi.org/10.1029/2005GL022690.
Tseng, W.-L., Ip, W.-H., Johnson, R.E., Cassidy, T.A., Elrod, M.K., 2010. The structure and time variability of the ring atmosphere and ionosphere. Icarus 206 (2), 382–389. http://dx.doi.org/10.1016/j.icarus.2009.05.019.
Vervack, R.J., Moses, J.I., 2014. Saturn's upper atmosphere during the Voyager era: Reanalysis and modeling of the UVS occultations. Icarus (submitted for publication). arXiv:1408.1746.
Waite, J.H. et al., 2005. Oxygen ions observed near Saturn's A ring. Science 307 (February), 1260–1262.
Winkelstein, P., Caldwell, J., Kim, S.J., Hunt, G.E., Moore, V., 1983. A determination of the composition of the saturnian stratosphere using the IUE. Icarus 54, 309–318.
Woods, T.N., 2008. Recent advances in observations and modeling of the solar ultraviolet and X-ray spectral irradiance. Adv. Space Res. 42 (5), 895–902. http://dx.doi.org/10.1016/j.asr.2007.09.026.
Woods, T.N. et al., 2000. TIMED solar EUV experiment. Phys. Chem. Earth C 25 (5–6), 393–396.
Woods, T.N. et al., 2005. Solar EUV experiment (SEE): Mission overview and first results. J. Geophys. Res. 110 (A1), A01312. http://dx.doi.org/10.1029/2004JA010765.
Zarka, P., 1985. Directivity of Saturn electrostatic discharges and ionospheric implications. Icarus 61, 508–520.
Zebker, H.A., Marouf, E.A., Tyler, G.L., 1985. Saturn's rings: Particle size distributions for thin layer models. Icarus 64, 531–548.